NANO LETTERS

LETTER

pubs.acs.org/NanoLett

Guided Three-Dimensional Catalyst Folding during Metal-Assisted Chemical Etching of Silicon

Konrad Rykaczewski,[*,†] Owen J. Hildreth,[‡] Ching P. Wong,[‡,§,∥] Andrei G. Fedorov,[⊥] and John Henry J. Scott[†]

[†]Material Measurement Laboratory, National Institute of Standards and Technology, Gaithersburg, Maryland 20899-8370, United States

[‡]School of Materials Science and Engineering, Georgia Institute of Technology, Atlanta, Georgia 30332, United States

[§]Faculty of Engineering, The Chinese University of Hong Kong, Hong Kong

[∥]Department of Electronics Engineering, The Chinese University of Hong Kong, Hong Kong

[⊥]G. W. Woodruff School of Mechanical Engineering, Georgia Institute of Technology, Atlanta, Georgia 30332, United States

S Supporting Information

ABSTRACT: In recent years metal-assisted chemical etching (MaCE) of silicon, in which etching is confined to a small region surrounding metal catalyst templates, has emerged as a promising low cost alternative to commonly used three-dimensional (3D) fabrication techniques. We report a new methodology for controllable folding of 2D metal catalyst films into 3D structures using MaCE. This method takes advantage of selective patterning of the catalyst layer into regions with mismatched characteristic dimensions, resulting in uneven etching rates along the notched boundary lines that produce hinged 2D templates for 3D folding. We explore the dynamics of the folding process of the hinged templates, demonstrating that the folding action combines rotational and translational motion of the catalyst template, which yields topologically complex 3D nanostructures with intimately integrated metal and silicon features.

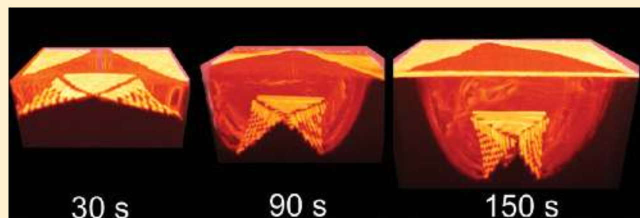

KEYWORDS: 3D nanofabrication, directed self-assembly, metal-assisted chemical etching, focused ion beam patterning

Applications of silicon nanostructures are becoming ubiquitous across a variety of technological fields. Integration of even the simplest shapes (e.g., straight nanowires) into electronic devices,[1,2] batteries,[3] thermoelectric devices,[4] biochemical sensors,[5] and photovoltaic cells[6,7] can significantly improve their performance. Further improvements could potentially be achieved by utilization of more complex structures, in terms of both attractive topological features and hybrid material combinations (e.g., metal−semiconductor composites). Quasi-three-dimensional nanostructures can in principle be made using modifications and combinations of traditional 2D fabrication techniques, such as bottom-up metal catalyzed vapor−liquid−solid (VLS) growth[8] or top-down lithographic and etching methods,[9−11] albeit with limited topological complexity. However, in order to fabricate complex 3D silicon nanostructures, more sophisticated methods need to be developed. In recent years metal-assisted chemical etching (MaCE) of silicon has emerged as a promising low-cost alternative to commonly used 3D fabrication methods[12] and has been successfully applied to produce tilted and zigzag nanowires,[13−15] helical holes,[16−18] and cycloidal[19] and spiral[19,20] trenches. In the MaCE process etching of silicon is confined to a small region surrounding a metal catalyst template that can travel in three dimensions as it etches into the silicon. In our recent work,[21,22] we demonstrated that the 3D motion of catalyst patterns during MaCE can be controlled by locally pinning them with an electrically insulating material[23] prior to etching. The pinning material acts as a fulcrum for rotation of the catalyst structures, resulting in etching of silicon features with rotational geometry. In this work we introduce a direct patterning process allowing for single step fabrication of 2D catalyst templates with multiple thicknesses. We demonstrate that a 2D metal catalyst film divided into adjacent regions with small and large characteristic dimensions is etched at different rates along the notched boundary lines, thus creating hinged catalyst substructures that act as templates for controllable folding of metal into 3D structures. We show that the folding process combines rotational and translational motion of the catalyst template and can be used to fabricate topologically complex 3D nanostructures with various orientations. Additionally, we utilize this new patterning process to gain fundamental insight into the influence of 2D catalyst template geometrical features on the MaCE etch rate.

In the MaCE process, gold, silver, or platinum nanoparticles or patterns etch locally into silicon when exposed to a solution containing redox mediators, such as H_2O_2 and HF. Silicon etching begins with catalytic reduction of H_2O_2 on the metal surface which creates a local cathode on the etchant side of the metal. This, in turn, injects holes into the valence band of silicon,

Received: March 3, 2011
Revised: April 20, 2011
Published: April 28, 2011

 © 2011 American Chemical Society

leading to a hole-enriched region of silicon (Si*) below the metal catalyst.[12,19,24] The holes are consumed at the HF/Si* interface by oxidation of Si^0 to Si^{4+} producing soluble SiF_6^{2-} and H_2SiF_6. The etching process continues as the catalyst structure travels into the regions where the silicon was removed, forming a mobile galvanic cell as the silicon is dissolved. With proper etchant composition, silicon dissolution is confined to a region in close proximity to the catalyst particle or pattern, creating high aspect ratio nearly straight holes protrusions in the silicon.[18,25,26]

Area-selective MaCE of silicon can be achieved by directly patterning metal nanoparticles and thin films using colloidal crystal or anodic aluminum oxide templating,[27−29] standard lithographic techniques,[9,19,20,30,31] microcontact imprinting,[32] superionic solid state stamping,[14] and focused ion beam induced deposition (FIBID).[21,33] Alternatively, area selective MaCE can be carried out by localized blocking of the etching using electron beam induced deposition (EBID) of a thin carbon layer beneath a nanoporous metal catalyst film.[23] In this work, we report that 2D catalyst metal substructures (etching templates) can be directly cut out of 50 nm thick uniform metal (Au) films using focused ion beam (FIB) milling (see Figure 1a). The depth to which the Au films are cut can be controlled by varying the local ion beam dose. For example, an ion beam dose of 85 pC/μm^2 results in a partial (≈35 to ≈45 nm) cut while a higher dose of 270 pC/μm^2 ensures full penetration of the Au layer and some of the underlying silicon. To complete the fabrication process, the Au templates are etched in a mixture of HF, H_2O_2, and methanol for a period of either 30, 90, 150, or 210 s (see Supporting Information for further experimental details). As demonstrated in Figure 1b and Figure 1c, nano- as well as microscale vertical structures can be fabricated by etching catalyst templates that have been perforated with small and large through-holes. The remaining part of the Au film adheres to and blocks the etching of the rest of the silicon surface. Some local deformation and occasional rupturing of the Au film occurs for etching times longer than 150 s (see Supporting Information for further discussion).

While there have been some reports of faster etching (downward motion) by smaller particles,[12] a systematic study of the influence of catalyst template geometry on the etching rate has not been performed. As shown in Figure 2, in this work we study the etching behavior of four sizes of square, circular, and rectangular Au templates, as well as seven varieties of perforated square Au templates. The geometry of the structures is designed so that the influence of the Au surface area and the characteristic length, defined as the ratio of the cut out gold surface area to edge distance, on the etch rate could be determined. The morphology of the etched structures is characterized by FIB cross sectioning and scanning electron microscopy (SEM) imaging. To avoid shape distortion due to direct ion beam exposure and indirect effects, such as material redeposition, the etched-out structures are filled with platinum using FIB induced deposition (see Supporting Information for further information on the cross-sectioning procedure). Typical results for etching the square templates of varied sizes are shown in Figure 2a, with corresponding etching depths at different times plotted for the smallest and largest squares in Figure 2e. Results for two sizes of rectangles and circles with similar areas are shown in Figure 2b and Figure 2c, while results for perforated squares are shown in Figure 2d. Initially all of the templates etch predominantly in a direction normal to the silicon surface; however, prolonged etching (>90 s) of the smaller or densely perforated

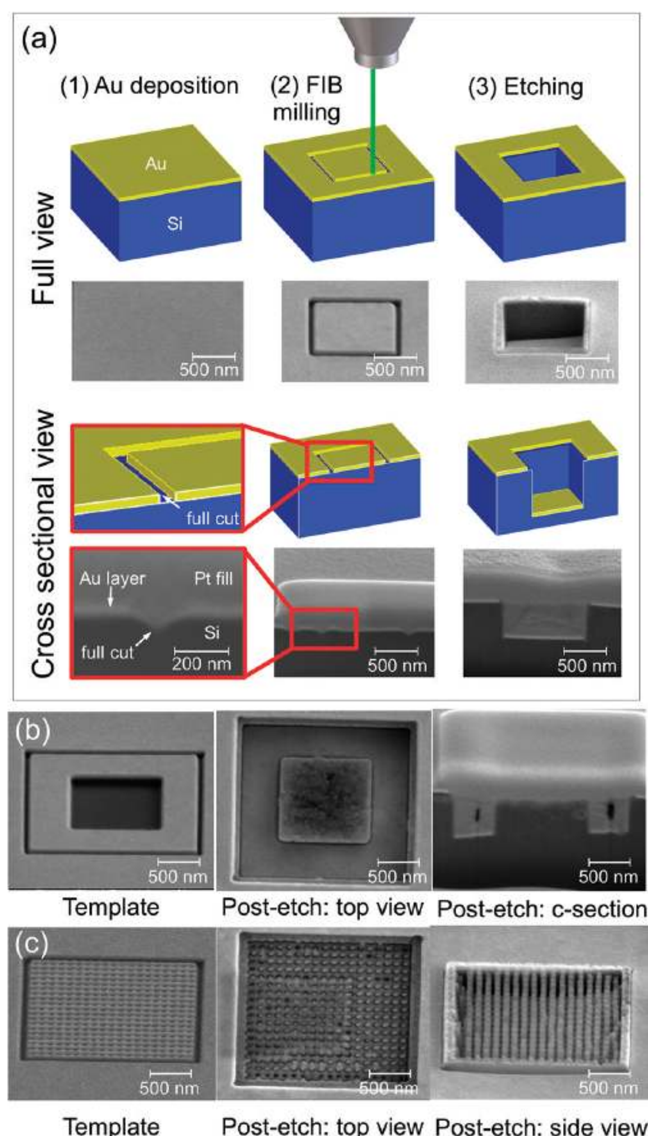

Figure 1. (a) Panoramic views and cross sectional schematics of the fabrication process consisting of Au film deposition, template definition via FIB milling of the Au film, and etching, along with representative SEM images. (b, c) Examples of FIB-milled perforated catalyst templates and resulting etched structures with (b) one large square hole producing a ≈500 nm tall micropillar after 90 s MaCE etch and (c) an array of 400 small circular holes producing an array of ≈500 nm tall nanowires after 30 s MaCE etch.

(thus mechanically weaker) Au templates sometimes results in their physical deformation and divergence from the vertical etching path. In agreement with results of previous studies,[12] we observe that the depth of etched-out features increases linearly with time for all structures. As a consequence, we use the etch rate as a criterion for comparison between the etching behavior of different Au templates. The etch rates are calculated using the variance-weighted least-squares method from the measured etch depth versus time data with exclusion of cross sections where the depth could not be determined due to nonvertical etch paths (for example, those seen in the cross section of 150 s nanowire template etching). The compiled results for etch rate plotted against the area and the characteristic dimension of all the tested Au templates are presented in panels

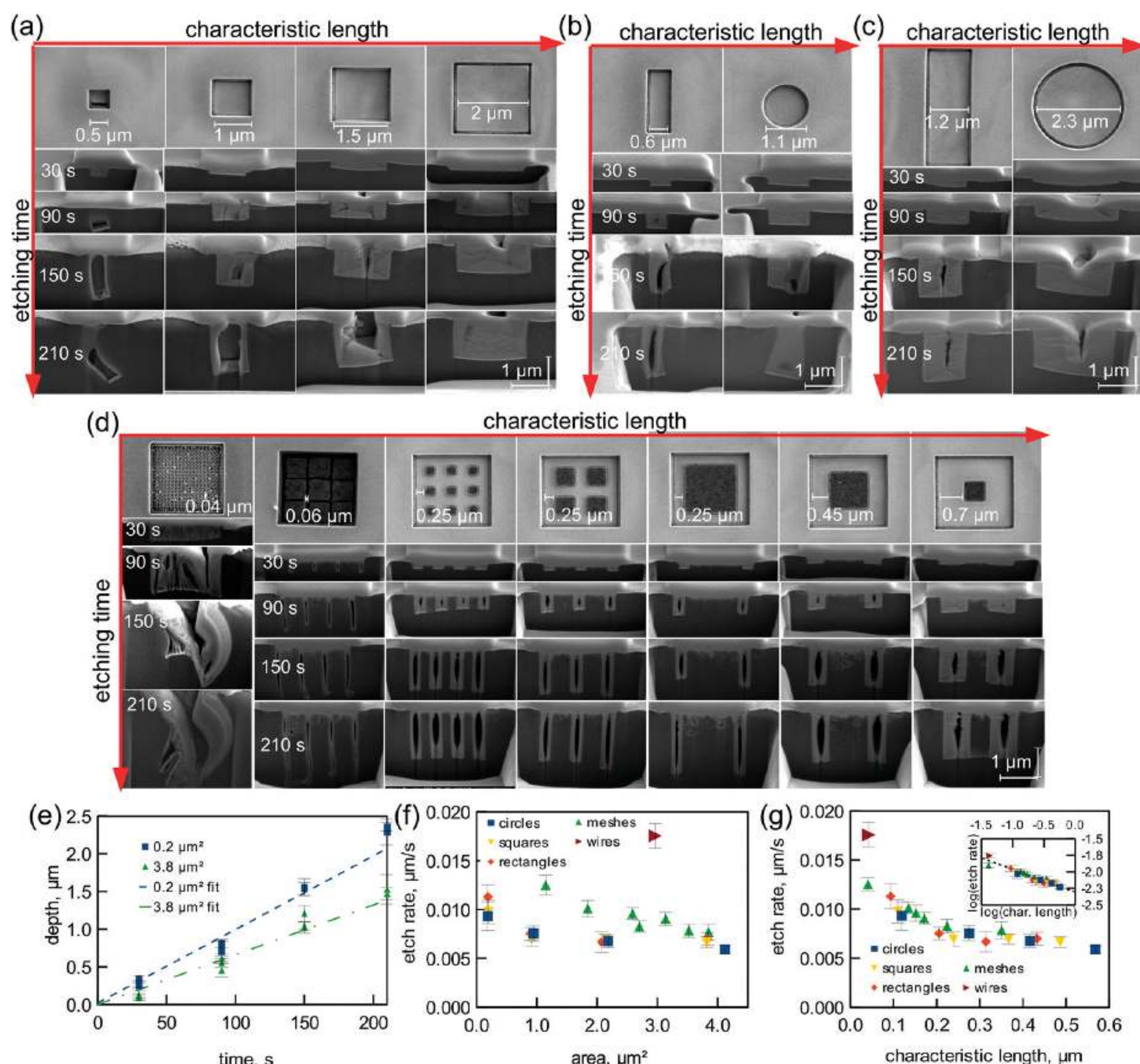

Figure 2. Influence of Au template geometry and size on etch rate: (a−d) Top and cross sectional SEM images of (a) ≈0.2 μm^2, ≈1 μm^2, ≈2.3 μm^2, and ≈4 μm^2 squares, (b) ≈1 μm^2 rectangle and circle, (c) ≈4 μm^2 rectangle and circle, and (d) ≈2 μm by ≈2 μm perforated squares with varied hole patterns etched for 30, 90, 150, and 210 s. (e) Plot of etched depth vs time and linear fits of the data corresponding to the etching of the smallest and largest squares in (a). (f, g) Plot of etch rate vs (f) total template area and (g) characteristic length of all tested structures. The insert in (g) shows a corresponding log−log plot.

f and g of Figure 2 (a tabulated form of the results is available in the Supporting Information). Etch rates for the uniform Au film templates with similar areas match regardless of the geometry (square, circle, or rectangle) and generally increase with a decrease in the area. However, etch rates for the perforated templates do not match the etch rates of the uniform film templates with similar areas, and the data are generally scattered suggesting that the catalyst-to-Si area is not appropriate for scaling. Furthermore, divergence of the etch rates for the uniform film templates and the perforated templates with large holes increases with decreasing total area. In contrast, when plotted against the characteristic length in Figure 2 g, the etch rates for the uniform film and the perforated structures match well and follow a consistent trend. Specifically, the etch rate scales with the inverse of the characteristic length raised to the one-third power (the exponent obtained from a linear fit of the log−log plot in Figure 2g is −0.345 ± 0.0524). The dependence of the etch rate on the characteristic length explains why the uniform film templates with similar areas but different characteristic dimensions greater than or near ≈0.25 μm, such as the circles and rectangles in Figure 2b,c, etch at similar rates. Comparing the etch rates of rectangles, squares, and circles with similar areas becomes difficult as the characteristic length falls below ≈150 nm. This is due to a large deviation of the vertical etching path which occurs during etching of small templates. Nevertheless, the choice of the characteristic length of the structures as the relevant geometrical feature which determines the MaCE etch rate is further illustrated by observations from the densely perforated nanowire templates, which exhibited an exceedingly fast etch rate (≈0.0175 μm/s or ≈1 μm/min). In this case, the total area was very large (≈3 μm^2) while the characteristic length is only ≈40 nm.

The etch rate of a Au template can be controlled by one or a combination of a number of processes involved in MaCE such as

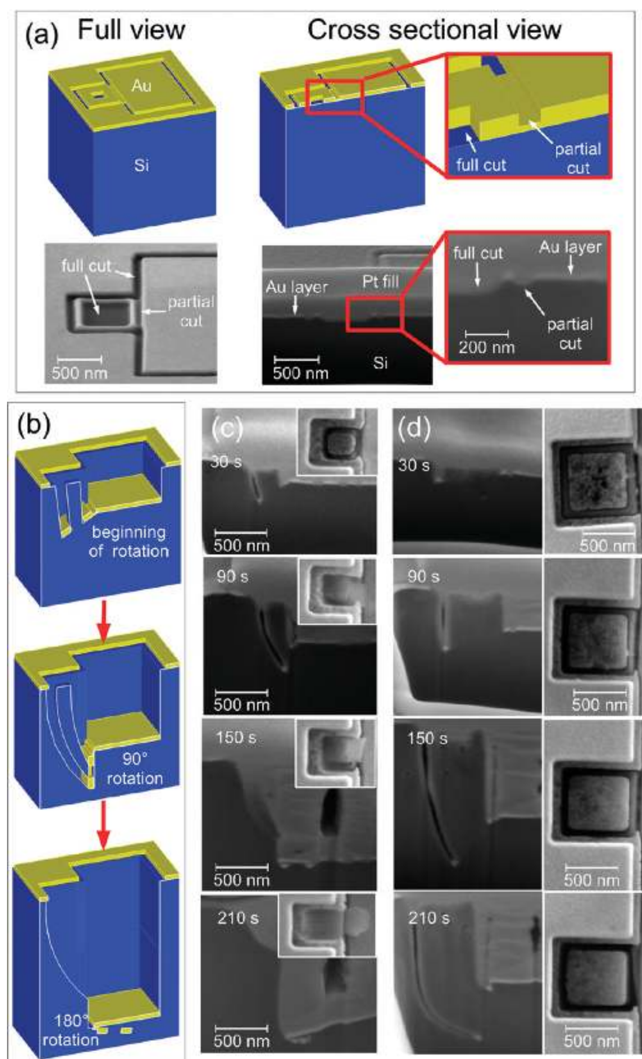

Figure 3. (a) Panoramic views and cross sectional schematics of a FIB-milled two part hinged Au template, along with representative SEM images. (b) Schematic representation of the two part hinged Au template folding dynamics. (c, d) Top and cross sectional SEM images demonstrating time progression of (c) small (350 nm side length) and (d) large (700 nm side length) perforated squares with a characteristic length of ≈60 nm folding around a ≈6 μm^2 uniform film square.

reagent supply to the etch site, electron and hole transport to the catalyst surface near the etching interface, or etch product removal. All of these processes should scale linearly with the size of the etched interface, which is proportional to the edge distance of the Au template. The total volume of the silicon removed during etching should scale directly with the area of the catalyst template. Thus is it not surprising that the etch rate shows a clear dependence on the characteristic length, which embodies both the edge distance and total surface area of the completely milled Au template. For the perforated square templates the decrease in the characteristic length is associated with a minor decrease in the surface area but a major increase in the edge distance. As a result of the increased length of the template edge there is a significant increase in the supply of the reagents near the etch site. The sharp increase in the etch rate associated with the characteristic length decrease, and with that enhanced access to reagent, indicates that the reagent supply is the likely mechanism controlling the etch rate for the present set of conditions.

Next we demonstrate that a combination of the capability for producing structures with desired etch rates (via adjusting of template geometric layout) and the local thinning of catalyst film by partial FIB milling provides a new option for fabrication of topologically complex 3D nanostructures. Specifically, we show that by segmenting a catalyst template via a notched boundary line into two parts with uneven etching rates, one can create a hinged template which controllably folds into a 3D structure during the MaCE etching process. Figure 3a shows an example of a hinged Au template consisting of a small perforated square and a large uniform film square (with corresponding small and large characteristic lengths that control the etch rate) separated by a partially FIB-milled or notched line (hinge). As shown in Figure 3b−d, as the entire template begins to etch vertically the smaller perforated part of the template etches faster and starts to fold around the hinge. Consequently, a silicon structure resulting from simultaneous rotational and translational motion of the perforated part of the template is fabricated. After the perforated part of the template rotates ≈90° about the hinge, the fabricated silicon pillar is cut off from the rest of the substrate by the edge of the vertically etching nonperforated (uniform film) part of the template. The folding motion continues until the perforated part of the template rotates ≈180°. During later stages of the etching process, the perforated part of the catalyst remains below the nonperforated part of the template while the entire structure continues to etch vertically. Comparison of results presented in panels c and d of Figure 3 shows that the angular velocity, ω, of the perforated part around the hinge increases with decreasing the side length, l, of the squares. For example, a 350 nm long perforated square completes the 180° rotation within 150 s, while a 700 nm long feature rotates only to ≈50° during the same period of time. If the etching velocity normal to the surface of the perforated part of the template at its outermost point, v_c, is constant and equal to the etching velocity of unconstrained templates with the same characteristic length, then $\omega \sim v_c/l$ for all values of l. While this relationship explains the rotational motion qualitatively, quantification of dynamics of the catalyst template folding is further complicated by other factors such as the vertical translational motion.

Having explored the folding behavior of two part hinged templates, we now turn to the etching behavior of more complex templates. As shown in Figure 4, our focus is on assembly of a large equilateral triangle separated into four parts by a set of three hinges. Short hinges divide the triangle into a polygon and three small equilateral triangles (Figure 4a), while longer hinges are designed to divide the large triangle into four equal size equilateral triangles (Figure 4b). To increase their etching rate, the characteristic length of the outer triangles is reduced by milling out a triangular area (Figure 4a,b) or a set of densely spaced small holes (Figure 4c) in their center. MaCE etching of these four-segment templates, shown in Figure 4, clearly demonstrates simultaneous folding of the outer triangles around the FIB-milled hinges toward the inner part of the template. The hinges act as three independent axes of rotation oriented at 60° with respect to each other. As expected, triangles with short side length rotate faster than those with the longer side length, while the large triangles perforated by a single large hole and array of small holes fold roughly at the same rate. Etching of templates with outer triangles perforated with single and multiple holes results in fabrication of three curved micropillars and three sets of curved nanowire arrays, respectively. The close-up SEM images in Figure 4c clearly demonstrate the unique curved geometry of

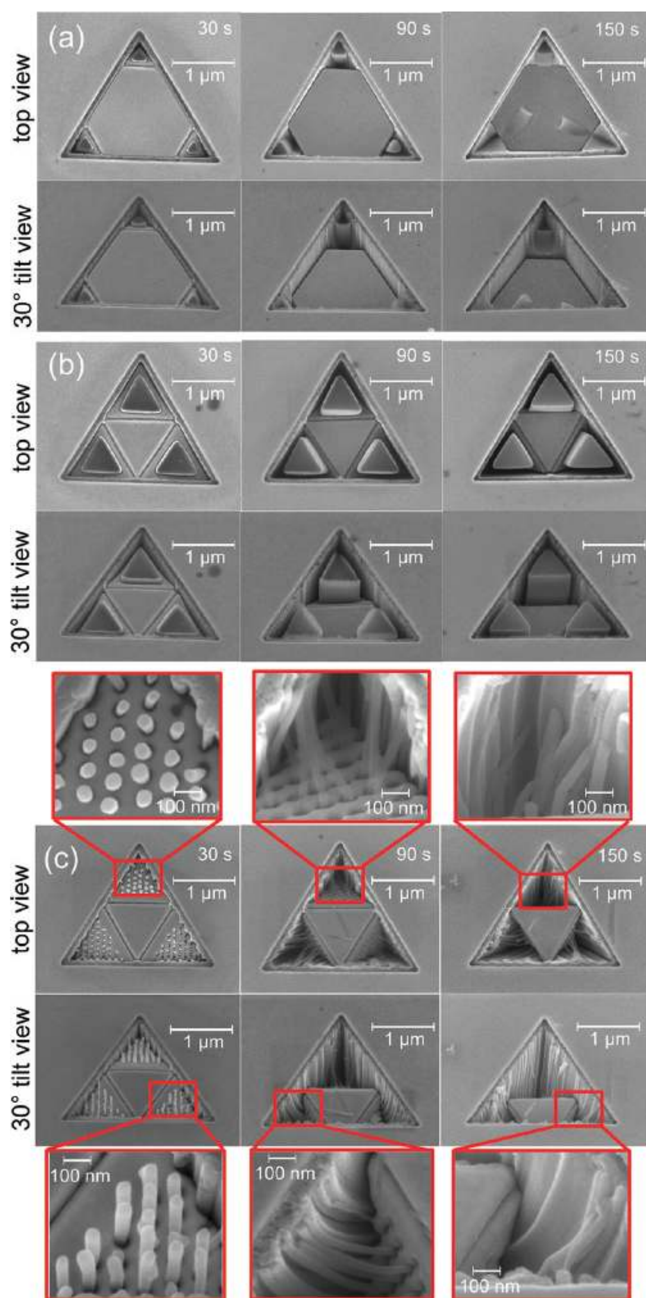

Figure 4. Top and 30° tilt SEM images of hinged Au templates with triangular features folding during etching: (a) ≈2.5 μm^2 triangle with three small (500 nm side length) outer equilateral triangular features perforated with single large holes; (b) ≈2.5 μm^2 triangle with three large (1000 nm side length) outer equilateral triangular features perforated with single large holes; (c) ≈2.5 μm^2 triangle with large (1000 nm side length) outer equilateral triangular features perforated with dense array of small holes.

the fabricated nanowires. The pillars as well as nanowires are cut away from the rest of the substrate after the outer triangles complete 90° rotation with respect to the inner part of the templates. Some of the nanowires also likely broke off during the water rinsing and nitrogen drying of the samples. The 3D nature of the folding process is revealed in the sequential FIB cross sectional slices and 3D reconstruction animations available in the Supporting Information. Lastly, as shown in Figure 4c, after 150 s of etching, the four triangle 2D templates nearly assemble into an inverted triangular pyramid or tetrahedron, suggesting that the method can be utilized to assemble a complex, stand-alone 3D metal object from the 2D templates during the etching process.

In summary, in this work we introduce a novel process in which 2D hinged Au templates controllably fold into 3D structures during MaCE of silicon. The process is enabled by the ability to produce templates and controllably define hinge points via FIB milling of the catalyst films to different thickness and shapes. Investigation of the etch rate of a portfolio of specially designed catalyst structures revealed the relevant characteristic length scale that allows one to control etch rate irrespective of the total area of the catalyst film. Armed with this fundamental understanding, we explored the dynamics of the hinged templates to demonstrate that the folding process combines rotational and translational motion, resulting in topologically complex 3D nanostructures combining the metal catalyst and silicon substrate. The introduced metal template folding process follows the same 2D-to-3D geometry transfer rules[34−37] (e.g., pattern-transfer of a 2D triangular template onto a 3D pyramid structure) as micro-[38−40] and nanoscale[41,42] self-assembly methods relying on stress-induced curvature. For completion of assembly of 3D structures, a physical interconnection or merging of individual folding components, analogous to the tin hinge fusing process,[41] could be achieved by edge milling into self-locking patterns.[37] The fabrication of topologically complex 3D silicon−gold composites introduced in this work should open up new opportunities for optical applications, such as fabrication of 3D photonic crystals,[43] and biological applications such as 3D scaffolds for control of cell growth and cell functions.[44−46]

■ ASSOCIATED CONTENT

S Supporting Information. Combined FIB catalyst milling and MaCE fabrication procedure details, FIB cross sectioning and imaging procedure details, gold film adhesion and damage during MaCE, and tabulated form of the data presented in Figure 2. This material is available free of charge via the Internet at http://pubs.acs.org.

■ AUTHOR INFORMATION

Corresponding Author
*E-mail: konrad.rykaczewski@nist.gov.

■ ACKNOWLEDGMENT

This research was performed while Dr. K. Rykaczewski held a National Research Council American Recovery and Reinvestment Act (NRC ARRA) Research Associateship Award at the National Institute of Standards and Technology in Gaithersburg, MD. A. G. Fedorov was supported by NSF Grant DMI 0403671.

■ REFERENCES

(1) Cui, Y.; Zhong, Z.; Wang, D.; Wang, W. U.; Lieber, C. M. *Nano Lett.* **2003**, *3* (2), 149–152.
(2) Goldberger, J.; Hochbaum, A. I.; Fan, R.; Yang, P. *Nano Lett.* **2006**, *6* (5), 973–977.
(3) Cui, L. F.; Ruffo, R.; Chan, C. K.; Peng, H.; Cui, Y. *Nano Lett.* **2008**, *9* (1), 491–495.

(4) Hochbaum, A. I.; Chen, R.; Delgado, R. D.; Liang, W.; Garnett, E. C.; Najarian, M.; Majumdar, A.; Yang, P. *Nature* **2008**, *451* (7175), 163–167.
(5) Cui, Y.; Wei, Q.; Park, H.; Lieber, C. M. *Science* **2001**, *293* (5533), 1289–1292.
(6) Kelzenberg, M. D.; Boettcher, S. W.; Petykiewicz, J. A.; Turner-Evans, D. B.; Putnam, M. C.; Warren, E. L.; Spurgeon, J. M.; Briggs, R. M.; Lewis, N. S.; Atwater, H. A. *Nat. Mater.* **2010**, *9* (3), 239–244.
(7) Peng, K. Q.; Wang, X.; Li, L.; Wu, X.-L.; Lee, S. T. *J. Am. Chem. Soc.* **2010**, *132* (20), 6872–6873.
(8) Park, W. I.; Zheng, G.; Jiang, X.; Tian, B.; Lieber, C. M. *Nano Lett.* **2008**, *8* (9), 3004–3009.
(9) Choi, W. K.; Liew, T. H.; Dawood, M. K.; Smith, H. I.; Thompson, C. V.; Hong, M. H. *Nano Lett.* **2008**, *8* (11), 3799–3802.
(10) Morton, K. J.; Nieberg, G.; Bai, S.; Chou, S. Y. *Nanotechnology* **2008**, *19* (34), 345301.
(11) Madou, M. J., *Fundamentals of microfabrication: The science of Miniaturization*, 2nd ed.; CRC: New York, 2002.
(12) Huang, Z.; Geyer, N.; Werner, P.; de Boor, J.; Gösele, U. *Adv. Mater.* **2010**, *23* (2), 285–308.
(13) Peng, K.; Lu, A.; Zhang, R.; Lee, S. T. *Adv. Funct. Mater.* **2008**, *18* (19), 3026–3035.
(14) Chern, W.; Hsu, K.; Chun, I. S.; Azeredo, B. P. d.; Ahmed, N.; Kim, K.-H.; Zuo, J.-m.; Fang, N.; Ferreira, P.; Li, X. *Nano Lett.* **2010**, *10* (5), 1582–1588.
(15) Chen, H.; Wang, H.; Zhang, X.-H.; Lee, C.-S.; Lee, S.-T. *Nano Lett.* **2010**, *10* (3), 864–868.
(16) Tsujino, K.; Matsumura, M. *Adv. Mater.* **2005**, *17* (8), 1045–1047.
(17) Tsujino, K.; Matsumura, M. *Electrochem. Solid State Lett.* **2005**, *8* (12), C193–C195.
(18) Tsujino, K.; Matsumura, M. *Electrochim. Acta* **2007**, *53*, 28–34.
(19) Hildreth, O. J.; Lin, W.; Wong, C. P. *ACS Nano* **2009**, *3* (12), 4033–4042.
(20) Chun, I. S.; Chow, E. K.; Li, X. L. *Appl. Phys. Lett.* **2008**, *92* (19), 3.
(21) Rykaczewski, K.; Hildreth, O. J.; Wong, C. P.; Fedorov, A. G.; Scott, J. H. J. *Adv. Mater.* **2010**, *23* (5), 659–663.
(22) Hildreth, O. J.; Wong, C. P. *Adv. Funct. Mater.* DOI: 10.1002/adfm.201100279.
(23) Rykaczewski, K.; Hildreth, O. J.; Kulkarni, D.; Henry, M. R.; Kim, S. K.; Wong, C. P.; Tsukruk, V. V.; Fedorov, A. G. *ACS Appl. Mater. Interfaces* **2010**, *2* (4), 969–973.
(24) Gorostiza, P.; Diaz, R.; Kulandainathan, M. A.; Sanz, F.; Morante, J. R. *J. Electroanal. Chem.* **1999**, *469* (1), 48–52.
(25) Chartier, C.; Bastide, S.; Levy-Clement, C. *Electrochim. Acta* **2008**, *53* (17), 5509–5516.
(26) Li, X.; Bohn, W. P. *Appl. Phys. Lett.* **2000**, *77* (16), 2572.
(27) Asoh, H.; Arai, F.; Ono, S. *Electrochem. Commun.* **2007**, *9* (4), 535–539.
(28) Asoh, H.; Arai, F.; Uchibori, K.; Ono, S. *Appl. Phys. Express* **2008**, *1* (6), 3.
(29) Huang, J.; Chiam, S. Y.; Tan, H. H.; Wang, S.; Chim, W. K. *Chem. Mater.* **2010**, *22* (13), 4111–4116.
(30) Chang, S. W.; Chuang, V. P.; Boles, S. T.; Thompson, C. V. *Adv. Funct. Mater.* **2010**, *20* (24), 4364–4370.
(31) Chang, S. W.; Chuang, V. P.; Boles, S. T.; Ross, C. A.; Thompson, C. V. *Adv. Funct. Mater.* **2009**, *19* (15), 2495–2500.
(32) Harada, Y.; Li, X. L.; Bohn, P. W.; Nuzzo, R. G. *J. Am. Chem. Soc.* **2001**, *123* (36), 8709–8717.
(33) Chattopadhyay, S.; Bohn, P. W. *J. Appl. Phys.* **2004**, *96* (11), 6888–6894.
(34) Schmidt, O. G.; Eberl, K. *Nature* **2001**, *410* (6825), 168–168.
(35) Prinz, V. Y.; Seleznev, V. A.; Gutakovsky, A. K.; Chehovskiy, A. V.; Preobrazhenskii, V. V.; Putyato, M. A.; Gavrilova, T. A. *Phys. E (Amsterdam, Neth.)* **2000**, *6* (1−4), 828–831.
(36) Boncheva, M.; Whitesides, G. M. *Adv. Mater.* **2005**, *17* (5), 553–557.
(37) Arora, W. J.; Nichol, A. J.; Smith, H. I.; Barbastathis, G. *Appl. Phys. Lett.* **2006**, *88* (5), 3.
(38) Tyagi, P.; Bassik, N.; Leong, T. G.; Cho, J. H.; Benson, B. R.; Gracias, D. H. *J. Microelectromech. Syst.* **2009**, *18* (4), 784–791.
(39) Stellman, P.; Buchner, T.; Arora, W. J.; Barbastathis, G. *J. Microelectromech. Syst.* **2007**, *16* (4), 932–949.
(40) Bassik, N.; Stern, G. M.; Jamal, M.; Gracias, D. H. *Adv. Mater.* **2008**, *20* (24), 4760–4764.
(41) Cho, J. H.; Gracias, D. H. *Nano Lett.* **2009**, *9* (12), 4049–4052.
(42) Cho, J. H.; James, T.; Gracias, D. H. *Adv. Mater.* **2010**, *22* (21), 2320–2324.
(43) Lezec, H. J.; Dionne, J. A.; Atwater, H. A. *Science* **2007**, *316* (5823), 430–432.
(44) Bettinger, C. J.; Langer, R.; Borenstein, J. T. *Angew. Chem. In. Ed.* **2009**, *48*, 5406–5415.
(45) Randall, C. L.; Kalinin, Y. V.; Jamal, M.; Manohar, T.; Gracias, D. H. *Lab Chip* **2011**, *11*, 127–131.
(46) James, T.; Cho, J. H.; Fernandes, R.; Randhawa, J. S.; Gracias, D. H. *Anal. Bioanal. Chem.* **2010**, *398* (7−8), 2949–2954.